Results from the Harmoni Laser Guide Star wavefront sensor prototype

Paul Rouquette, Pierre Jouve, Anne Costille, Benoit Neichel, Kjetil Dohlen, Felipe Pedreros Bustos, Thierry Fusco

Results from the the Harmoni Laser Guide Star wavefront sensor prototype

Paul Rouquette*[a], Pierre Jouve[b], Anne Costille[a], Benoit Neichel[a], Kjetil Dohlen[1], Felipe Pedreros Bustos[c], Thierry Fusco[b]
[a]Aix Marseille Université CNRS CNES, LAM (Laboratoire d'Astrophysique de Marseille) UMR 7326, Marseille, France
[b]ONERA, Chatillon, France
[c]European Southern Observatory, Garching bei Munchen, Germany

ABSTRACT

The impact of the microlens profiles on the optical adaptative performances of the Harmoni LGSS is analyzed. Starting from measurements of microlens surfaces, an optical model has been developed that allows to get light intensity distribution on the detector. Spots positions are then detected by a weighted center of gravity. The noise associated to this measure is simulated and studied as a function of flux and weighted function. A comparison with ideal lenses is provided which gives the following result: with the microlenses studied in this article, around 1.6 times more photons are needed to get the same precision in the detection of the spot than with ideal ones.

Keywords: Harmoni, LGSS, Shack-Hartmann, Microlens, Weighted Center of Gravity, Centroiding, Photon and Read-Out noise.

1. INTRODUCTION

HARMONI is the first light visible and near-IR integral field spectrograph for the ELT that will be on sky on 2029. To prepare the final design of the Laser Guide Star Sensors (LGSS)[1], we have developed since few years a full-scale prototype implemented in an optical bench.

The WaveFront Sensor is a classic Shack-Hartmann composed of 80x80 double side microlens array, a 6 lenses optical relay to reimage the light coming from the microlenses on the detector, and a CMOS camera using a SONY detector with 1608x1104 pixels, RON < 3e- at a frame rate of 500Hz. The choice of the sensor has been motivated by the large number of pixels to provide a field of view larger than 15 arcsec per subaperture.

As a result of the manufacturing process, the shape of the microlenses has physical defects, particularly in the transition zone between two microlenses. This automatically leads to optical aberrations in the system. The question that naturally arises is what are their impact on the optical adaptative process.

To answer to this question, the first step is to characterize the impact of the aberrations on the detection of the position of the spots on the detector. This is the scope of this article where an optical model of microlenses along with a centroiding study have been developed.

2. OPTICAL MODEL OF A MICROLENS

In order to characterize the impact of the microlenses, we have developed a simple optical model based on four main steps. This allows to get the distribution of light on the camera that will be used in the centroiding study in section 3.

2.1 Phase Modellling

The first step is to model the phase introduced by a microlens. To do so, we start from measurements of the microlens surface, as shown in Figure 1 a), and which has been realized with a Wyko NT 9100 Optical Profiling System. A sphere is then fitted to this surface and the result is presented in Figure 1 b) where the µlens altitude is plotted in red and the fitted

curve in blue. The surface deviates significantly from the sphere on the edges due to the presence of adjacent lenses and manufacturing errors.

The optical path difference between a straylight that passes through the microlens and a one that goes through the ideal sphere is:

$$\Delta = (n-1)\left(z_{\mu\text{lens}} - z_{\text{sph}}\right) \quad (1)$$

where $z_{\mu\text{lens}}$, z_{sph} are the altitude of the microlens and the sphere, and n is the optical index of the lens.

Figure 1 c) shows the phase expressed in radian and calculated from this optical path difference with a wavelength of 589 nm corresponding to the one of the Laser Guide Star (LGS). The phase in 1D is also plotted in Figure 1 d) at y=0. The microlens introduces strong phase values (greater than 10 radians) on the edges of the microlens.

Note that only one side of the lens has been considered.

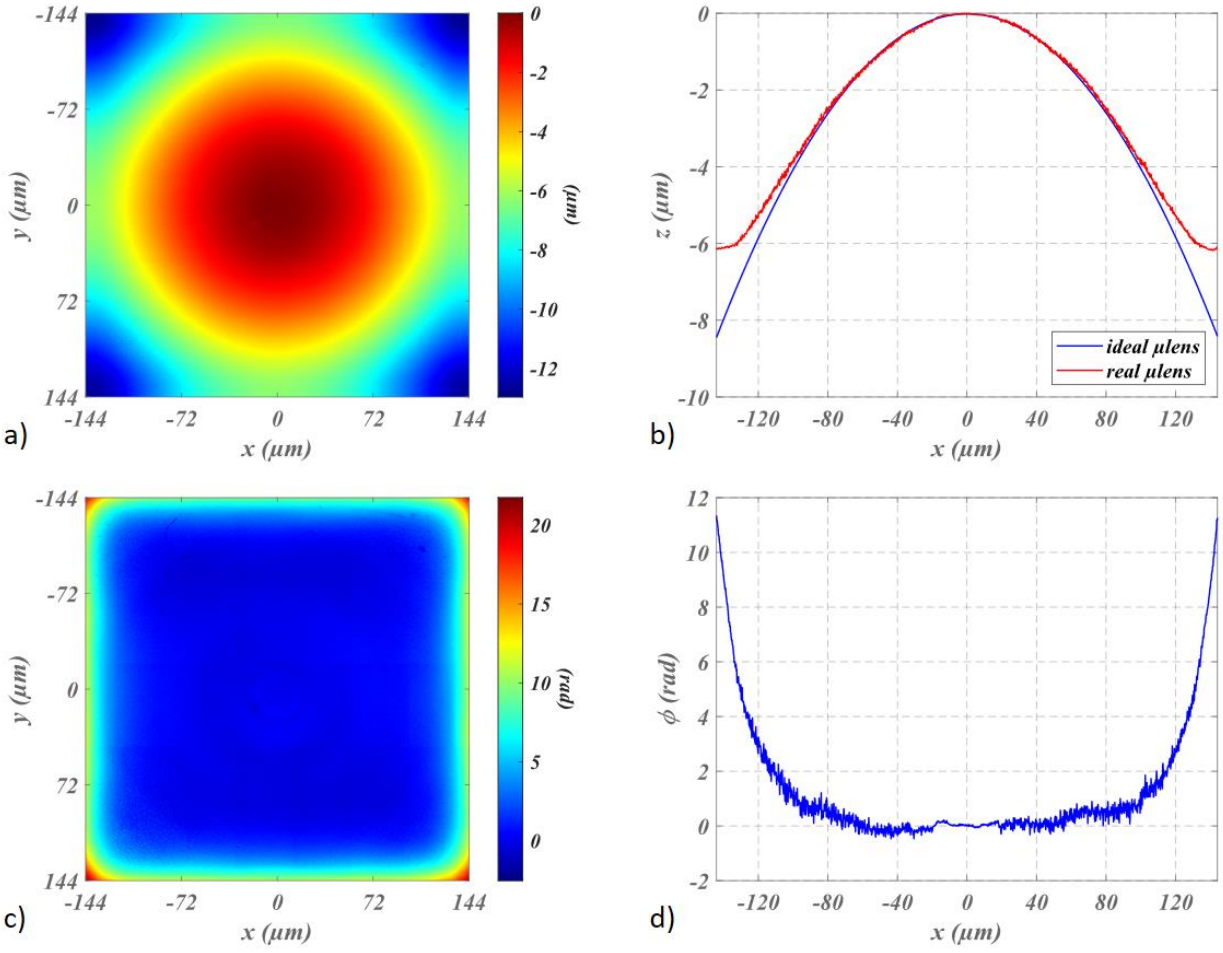

Figure 1: a) altitude profile of a microlens. The center of the lens corresponds to the point $(x, y) = (0,0)$. b) altitude profile along the x-axis at $y = 0$ of the lens (red) and the fitted sphere (blue). c) phase difference introduced by the lens in radii. d) phase along the x-axis at $y = 0$.

2.2 PSF estimation

We will now study the impact of the phase on the distribution of light in the focal plane. It is well-known that electric field in pupil and focal plane are linked with a simple Fourier Transform (FT).

We start from the expression of the electric field in pupil plane which can be written as:

$$E(x,y) = P(x,y)e^{j\phi(x,y)} \tag{2}$$

where ϕ is the phase introduced by the lens (see section 2.1) and $P(x,y) = \text{Rect}\left(\frac{x}{d}\right)\text{Rect}\left(\frac{y}{d}\right)$ is the pupil function associated to the lens. The parameter d is the lateral dimension of the lens (which is a square).

The image of a point source by this lens, the point spread function (PSF), is proportional to the square modulus of the Fourier Transform of equation (2). We can write:

$$PSF(f_x, f_y) = \left|FT\{Pe^{j\phi}\}(f_x, f_y)\right|^2 \tag{3}$$

where (f_x, f_y) are the Fourier variables conjugated to (x, y).

In Figure 2, the PSF of three different lenses are shown. Figure 2 a) corresponds to the ideal lens when $\phi = 0$, in other words the diffraction of the lens. Figure 2 b) corresponds to the real microlens with the phase calculated in section 2.1. Figure 2 c) shows the PSF measurements realized at IPAG (Institut de Planétologie et d'Astrophysique de Grenoble) using a microscope. Finally, Figure 2 d) shows the three previous case as a function of the x-axis. Note that the PSF of the real lens have "wings" that contributes to spread lights on both axes.

All PSF have been normalized in energy. Axes are plotted in arcsec and correspond to the field of view on sky of the subaperture.

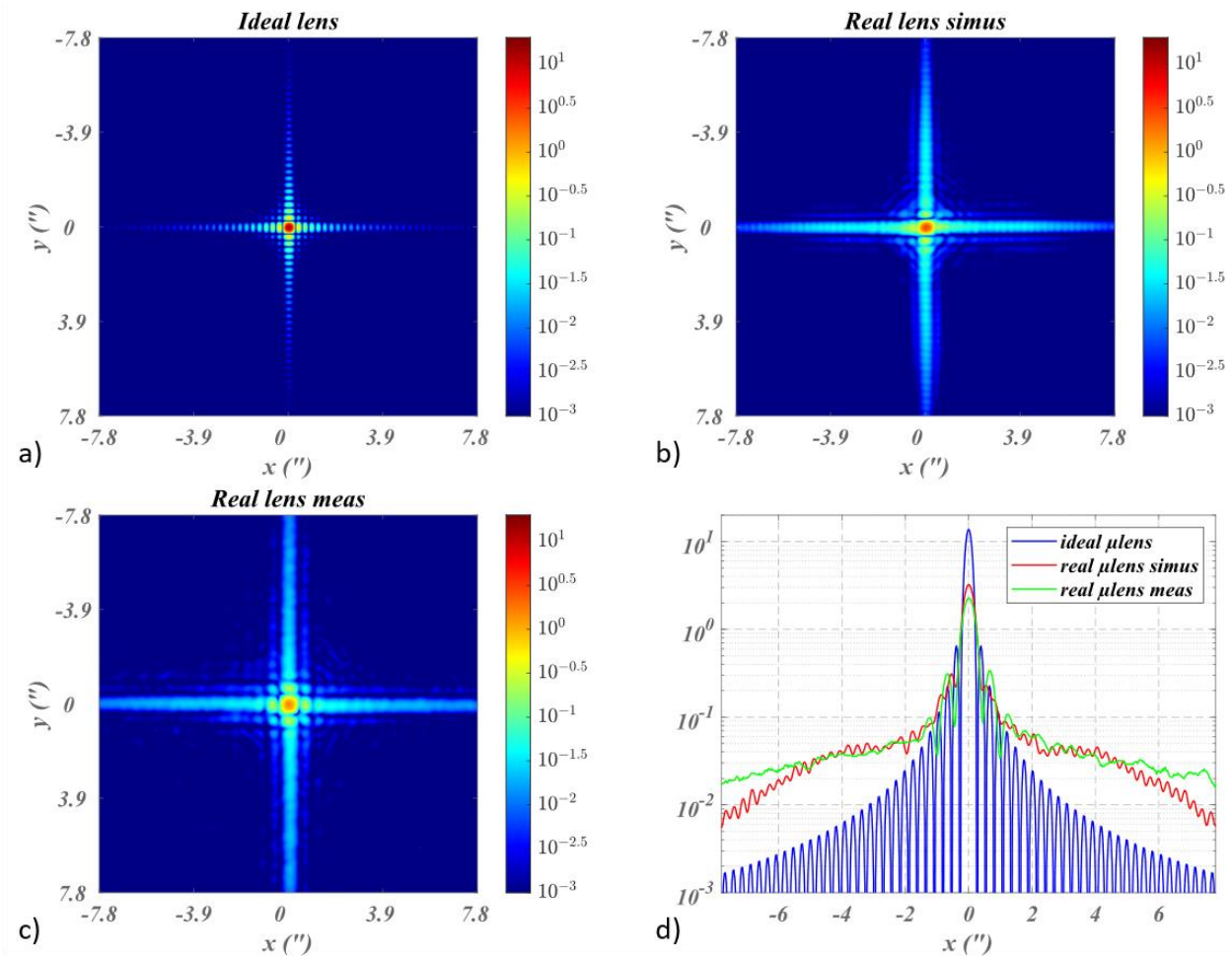

ed

Figure 2: a) PSF of the ideal lens. b) PSF of the real lens calculated with the phase determined in section 2.1. c) PSF measurements. d) comparison along the x-axis ($y = 0''$).

Two conclusions can be deduced from Figure 2. First, it validates our model since the green and red curves are similar. Second, the phase aberrations introduced by the lenses shift a certain amount of light from the central spot to higher frequencies.

2.3 Spot intensity: convolution by LGS

The microlens array will be used in the Shack Hartmann of the LGSS. It will therefore not image a source point but a LGS which can be represented by a Gaussian function with a full width half maximum (FWHM) of 1.2". It is then necessary to convolve the PSF obtained in section 2.2 by a Gaussian function. Equation (4) represents the intensity profile in the focal plane:

$$I = PSF * I_0 \quad \text{and} \quad I_0 = \frac{4\ln 2}{\pi L_0^2} e^{-\frac{4\ln 2}{L_0^2}(x^2+y^2)} \tag{4}$$

where L_0 is the FWHM (chosen at 1.2" for our analysis) of the LGS.

Results are shown in Figure 3. For computational reasons the spots are centered in $(10'', 10'')$. Figure 3 a,b,c) show respectively the LGS, the LGS convoluted by the PSF of the ideal lens (diffraction) and the LGS convoluted by the PSF of the real lens. The spots are also plotted against the x axis in Figure 3 d). All curves are normalized in energy. The "wings" shown in Figure 2 are clearly visible.

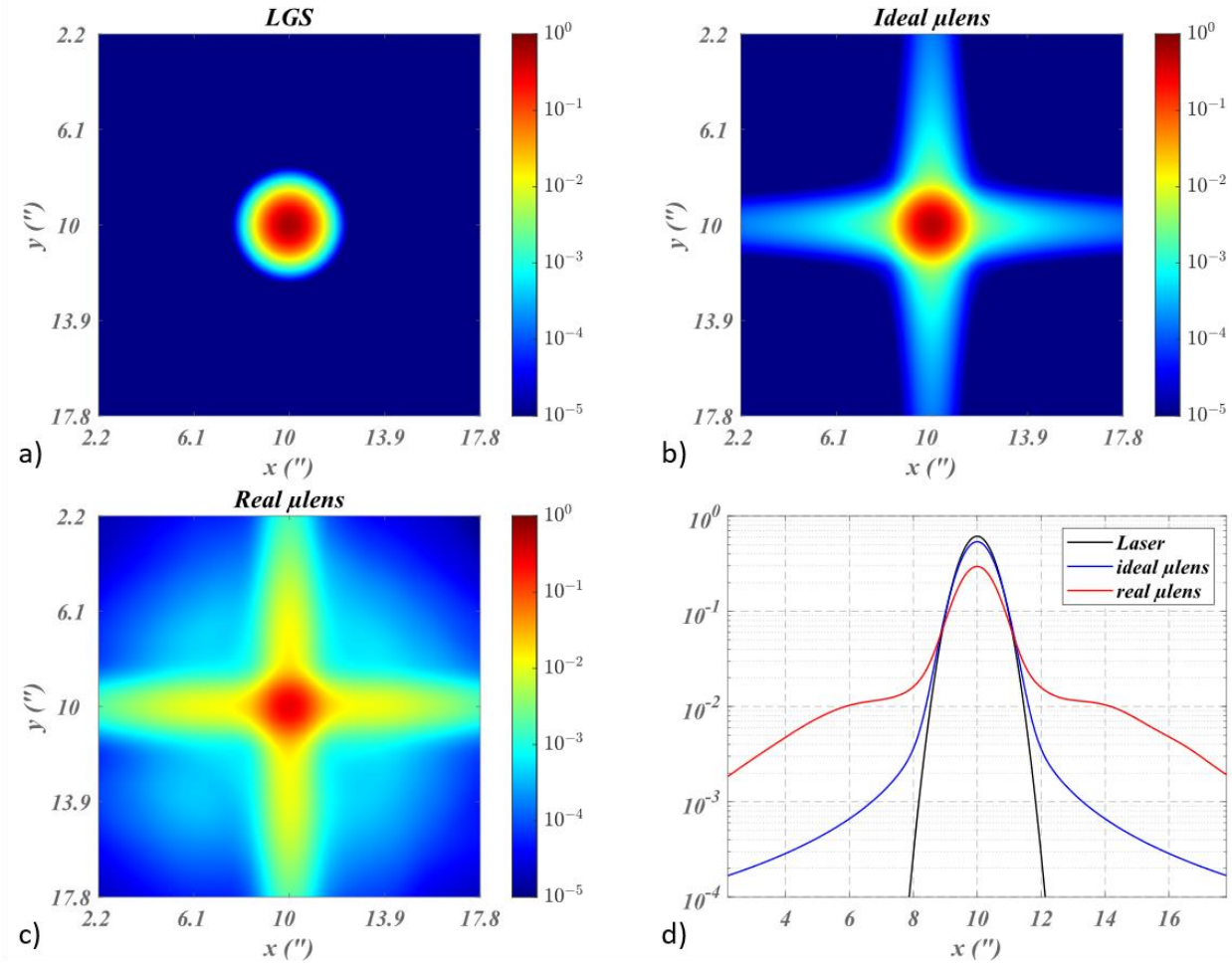

Figure 3: a) spot intensity of LGS (gaussian with FWHM = 1.2"). b) Convolution between the PSF of the ideal lens and the LGS. c) convolution between the PSF of the real lens and the LGS. d) spot intensities along the x-axis.

2.4 Sampling by the detector

In order to obtain the light distribution that will be used in the centroiding study (section 3), the last step is the sampling by detector. In the LGSS of Harmoni, a detector with 13*13 pixels per subaperture has been chosen. The width of a pixel represents 1.2″ on sky. This leads to the Figure 4 which represents the different intensity profiles of a) the LGS, b) the LGS convolved with the PSF of an ideal lens and c) the LGS convolved with the PSF of a real lens. Lastly the sampled spots are plotted against the x-axis on Figure 4 d). Note that the pixel arrangement has been chosen so that the center of the spot is between 2 pixels.

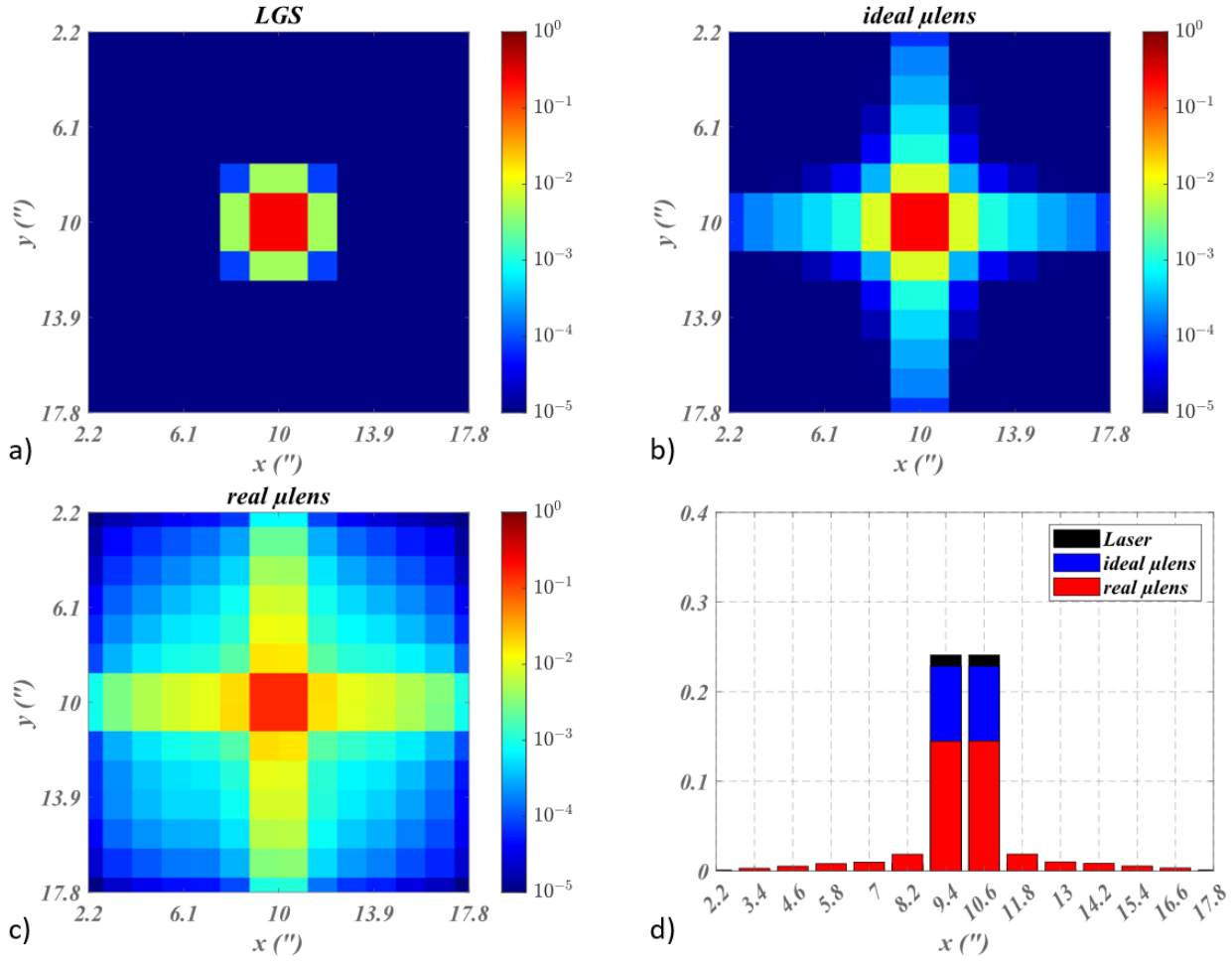

Figure 4: spot intensities of Figure 3 after sampling by the detector. The detector is composed of 13*13 pixels. The width of each pixel is 1.2".

3. CENTROIDING STUDY WITH WEIGHTED CENTER OF GRAVITY

3.1 Theoretical background

To detect the position of the spot on the detector, a weighted center of gravity[2] (WCoG) has been chosen. This method performs well in both the photon noise (PN) and read-out noise (RON) regimes. It consists in multiplying the spot intensity by a gaussian function and then doing a classical center-of-gravity measurement.

For the sake of simplicity, the WCoG will be analyzed along the x-axis only. It can be expressed as a function of spot intensity and weighted gaussian function[2]:

$$C_x = \frac{\sum_{i,j} x_{ij} I_{ij} W_{ij}}{\sum_{i,j} I_{ij} W_{ij}} \tag{5}$$

where x_{ij} is the position in arcsec on the x-axis of pixel (i,j) and I_{ij}, W_{ij} are the associated spot intensity and weighted function.

The weighted function W is centered on the center of the detector since the real position of the spot is not known a-priori. This leads to an error on the estimation of the position of the spot and the WCoG needs to be debias[2]. Expression (5) becomes:

$$C_x = \frac{1}{b}\frac{\sum_{i,j} x_{ij} I_{ij} W_{ij}}{\sum_{i,j} I_{ij} W_{ij}} \text{ with } b = \frac{L_W^2}{L_W^2 + L_0^2} \tag{6}$$

where L_W and L_0 are the FWHM of weighted function and spot intensity (both supposed gaussian).

Noise causes statistical error on the measurements. As photon and read out noise have zero mean value, the error is characterized by a standard deviation σ_x^2 which can be expressed analytically in case of gaussian spot intensity[2,3]. We have:

$$\sigma_x^2 = \frac{1}{b^2}\left(\underbrace{\frac{L_0^2 (L_W^2 + L_0^2)^2}{8\ln(2)\, N_{ph} (L_W^2 + 2L_0^2)^2}}_{PN} + \underbrace{\frac{\pi \sigma_{RON}^2 (L_W^2 + L_0^2)^2}{128\left(\ln(2)\, N_{ph}\right)^2} \frac{1}{d_{pix}^2}}_{RON} \right) \tag{7}$$

with N_{ph}, L_0, L_W the number of photons/subaperture/frame, the FWHM of spot intensity and weighted function. σ_{RON} is the standard deviation of RON and d_{pix} is the dimension of a pixel in arcsec fixed at 1.2" (see section 2.4).

This statistical error is the criterion that will be used to characterize the impact of microlenses on the detection of the position of the spot. The following study is carried on:

1) The spots represented in Figure 4 are multiplied by the number of photons arriving on each subaperture of the Shack Hartmann between two frames of the detector. This number is generally between 100 and 10000 photons/subaperture/frame.
2) Photon noise (PN) and read-out noise (RON) are then added. PN is represented by a Poisson process with parameter N_{ph}. RON is represented by a gaussian process with zero mean and standard deviation $\sigma_{RON} = 2.5e^-$. This value is in the order of magnitude of what has been measured on the CMOS detector[3] of the Harmoni LGSS prototype.
3) Centroiding is then realized by using the WCoG described above. The FWHM of weighted function has to be optimized (see section 3.2) before analyzing the results against the flux (see section 3.3).

3.2 Optimization of the FWHM of the weighted function

In this section the FWHM of the weighted function is optimized at fixed flux. PN and RON are added to the images of Figure 4. Then the weighted center of gravity is calculated over 10000 simulations to get the standard deviation of the measurement.

In Figure 5 a), the standard deviation of WCoG is presented as a function of the FWHM of the weighted function L_W for $N_{ph} = 1000$ photons/subaperture/frame. Recall that the FWHM of the LGS is fixed at $1.2''$. As before three cases are considered: the LGS alone (black), the ideal microlens (blue) and the real one (red). In addition, the theoretical curves from equation (6) are shown.

There is a value for L_W that minimizes the error on the measurement. This value is basically the same for the three cases and will be fixed at $L_W = 3.2''$ for the rest of the article. It also depends on the flux as shown in Figure 5 b) where the standard deviation of WCoG for different flux and for the real microlens only is plotted. As the number of photons decreases, the read-out noise becomes predominant and the optimum shifts towards smaller L_W.

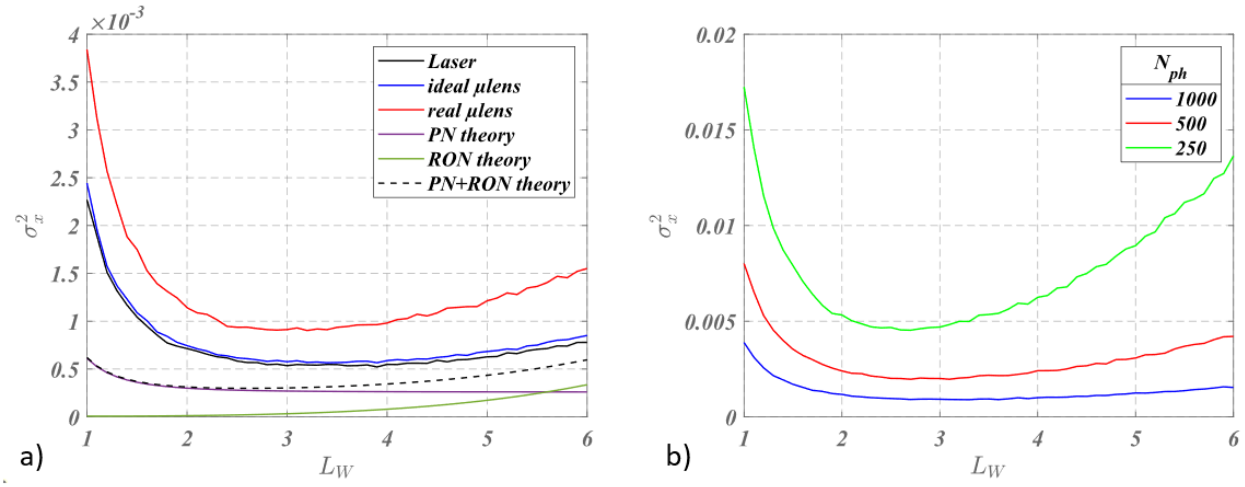

Figure 5: a) standard deviation of the WCoG simulations of the LGS, the LGS with ideal lens and the LGS with real lens, as a function of the FWHM of the weighted function with 1000 photons/subaperture/frame. b) same curves but for the real lens only and at different flux.

The under sampling of the spots (Shannon/2) introduces a static error which is responsible of the differences with theoretical curves. Figure 6 shows the same results but with a sampling at Shannon (with a detector of 25*25 pixels of 0.6" each). It shows the good agreement between theory and simulation.

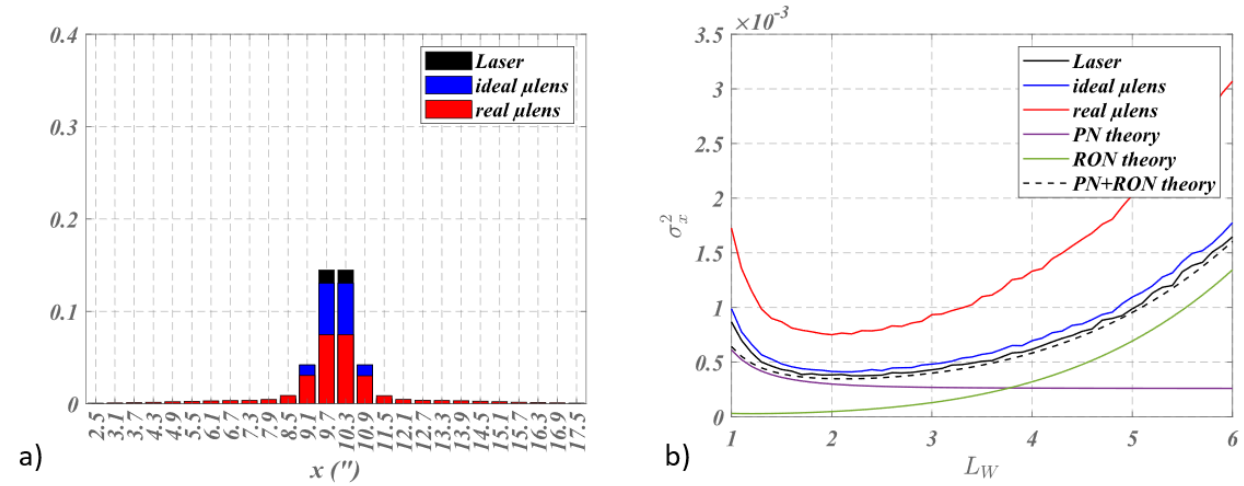

Figure 6: a) same as Figure 4 d) but with a sampling at Shannon. b) same as Figure 5 a) but with a sampling at Shannon.

3.3 Flux variation

As the FWHM of the weighted gaussian function has been optimized (section 3.2) and fixed at 3.2″, the following step consists in analyzing the performances as function of the flux. This is done in Figure 7 a) where the standard deviation of the WCoG has been plotted for the LGS, the ideal and the real microlens.

The results are in good agreement with the theory. As explained in section 3.2, differences come from the under sampling of the spots. For small flux (<200 photons/subaperture/frame), the RON dominates and the error is proportional to $1/N_{ph}^2$ whereas for higher flux PN dominates with an evolution in $1/N_{ph}$.

Figure 7 b) shows a comparison between the ideal and real microlens. The ratio between their standard deviations is presented as a function of the flux. It is comprised between 1.8 for small flux and 1.6 for higher ones. This is the main result of the article: with the microlens around 1.6 times more photons are needed to get the same precision in the detection of the spot than with ideal ones.

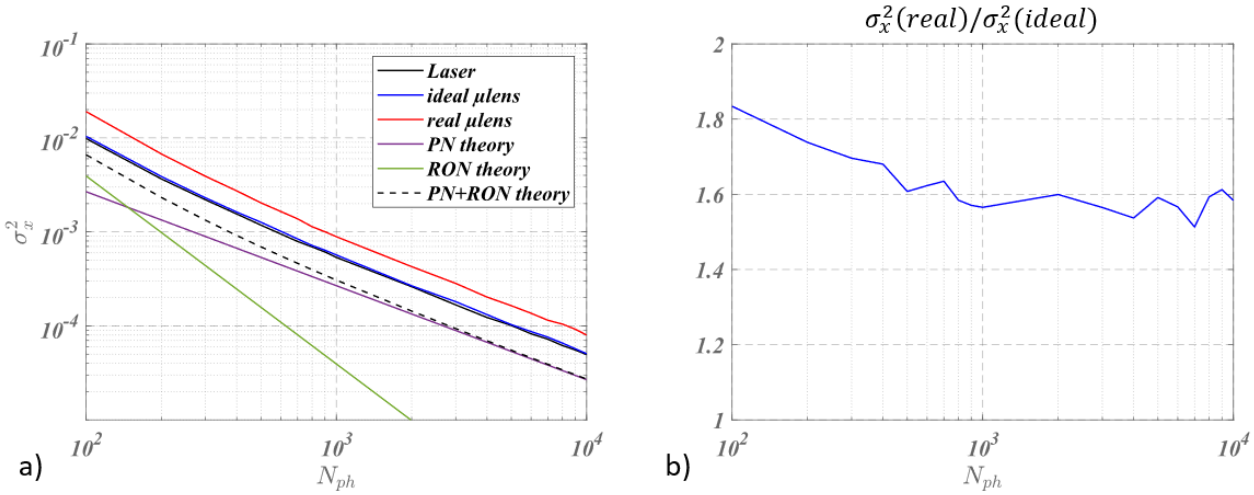

Figure 7: a) standard deviation of the WCoG simulations of the LGS, the LGS with ideal lens and the LGS with real lens, as a function of the flux (number of photons/subaperture/frame) b) ratio between the real and the ideal lens.

3.4 Masking of microlenses

This section presents a strategy that might at first sight improves the performance of microlenses. Since the main phase aberration is due to the side of the microlens, a reasonable idea could be to physically mask those parts.

To test this idea, Figure 8 shows the standard deviation of WCoG calculated with the real lens as function of the masking factor F_m and at three different flux. The curve is divided by the standard deviation calculated without masking and with ideal microlens. The F_m factor is defined as the surface area of the microlens that is masked. As can be seen, performances are not improved for $F_m \in [0\ 25]\%$ and even decreases after. This is because although phase aberrations decrease with increasing masking, the number of photons also decrease, thereby degrading performance. The two effects offset each other, and performance does not improve.

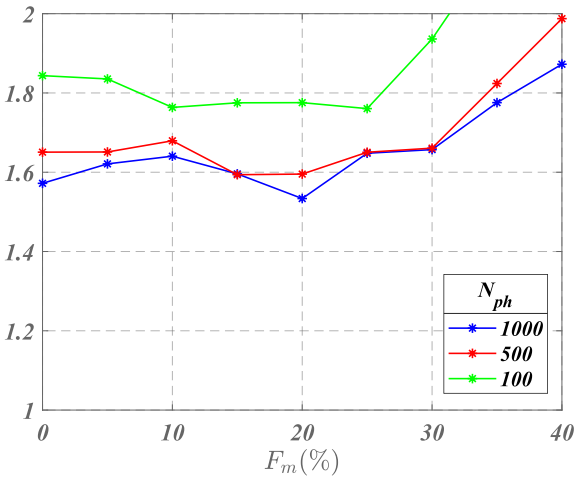

Figure 8: noise against masking for three different flux. The curves are the ratio σ_x^2 of the real lens with σ_x^2 of the ideal lens with no masking. The masking factor F_m is defined as the percentage of surface area that is masked.

It is interesting to note that masking is in fact already achieved numerically by the weighted function. As it has already been optimized, physical masking is useless and is therefore not a solution.

4. CONCLUSION

A numerical model has been conceived to characterize the impact of the microlens shape on the precision in the detection of the spot position by the detector. The main result is the following: around 1.6 times more photons are needed to get the same precision than with ideal microlens.

The noise introduced by the microlenses is due to manufacturing error and more specifically to the transition zone between two lenses. However, masking this zone does not reduce the noise as the weighted center of gravity acts already as the optimal numerical mask.

Works are currently underway to insert this result in LTAO end-to-end simulation in order to determine the impact of microlens on the final performance of the adaptive optic system of Harmoni.

REFERENCES

[1] Costille, A., Bonnefoi, A., Renault, E., Ceria, W., Dohlen, K., Neichel, B., Hubert, Z., Correia, J.-J., Moulin, T., Menendez Mendoza, S., Fusco, T., Pedreros Bustos, F., Jouve, P., El Hadi, K., Barboza, S., Rohloff, R.-R., Muller, F., Clarke, F., Schnetler, H., et al., "HARMONI at ELT: designing a laser guide star wavefront sensors for the ELT," Adaptive Optics Systems VIII, D. Schmidt, L. Schreiber, and E. Vernet, Eds., 172, SPIE, Montréal, Canada (2022).

[2] Thomas, S., Fusco, T., Tokovinin, A., Nicolle, M., Michau, V. and Rousset, G., "Comparison of centroid computation algorithms in a Shack-Hartmann sensor: Comparison of centroid computation algorithms," Monthly Notices of the Royal Astronomical Society **371**(1), 323–336 (2006).

[3] Ke, Z., Bustos, F. P., Atwood, J., Costille, A., Dohlen, K., El Hadi, K., Gach, J.-L., Herriot, G., Hubert, Z., Jouve, P., Rabou, P., Veŕan, J.-P., Wang, L., Fusco, T. and Neichel, B., "Performance of a complementary metal-oxide-semiconductor sensor for laser guide star wavefront sensing," J. Astron. Telesc. Instrum. Syst. **8**(02) (2022).